COMMUNICATION

Check for updates

Multichannel nitrogen-doped carbon fiber confined Fe₃C nanoparticles for efficient electroreduction of nitrate†

Fangzhou Zhang,[a] Zhangsheng Shi, [ID][c] Junliang Chen,[a] Hongxia Luo,[a] Jun Chen [ID] *[b] and Jianping Yang [ID] *[a]

Electrochemical conversion of nitrate into benign dinitrogen is a promising solution for water purification and environmental remediation. The development of environmentally friendly electrocatalysts possessing excellent catalytic activity and stability has attracted increasing attention. Herein, a 1D hierarchical architecture with uniformly dispersed Fe₃C nanoparticles confined in multichannel nitrogen-doped carbon fibers (Fe₃C/MNCFs) is reported as a highly efficient NO₃RR electrocatalyst. Fe₃C/MNCFs-800 demonstrates a nitrate conversion of 90.9%, an N₂ selectivity of 99.53%, and up to 15 cycles of electrocatalytic stability. The excellent electrocatalytic activity is proposed to be mainly due to the multichannel fibrous architecture beneficial for exposing more active sites and facilitating mass diffusion. Moreover, the strong interaction between active species and fibrous support guarantees the chemical stability and long cycle life. This work provides a reference for the development of high-performance noble-metal-free electrocatalysts for eco-friendly nitrate reduction.

Broader context

Nitrate is widely distributed in industrial wastewater, nuclear wastewater, and contaminated groundwater, which has increasingly provoked ecological and environmental concerns. The electrochemical nitrate reduction reaction (NO₃RR) has emerged as a promising approach for converting NO₃⁻ into harmless product N₂. It is indispensable to develop electrocatalysts with higher catalytic activity and selectivity for the NO₃RR. In this study, we report a novel 1D hierarchical architecture with uniformly dispersed Fe₃C nanoparticles confined in multichannel nitrogen-doped carbon fibers (Fe₃C/MNCFs) as an efficient NO₃RR electrocatalyst. Fe₃C/MNCFs-800 demonstrates a nitrate conversion of 90.9%, an N₂ selectivity of 99.53%, and up to 15 cycles of electrocatalytic stability. This work provides new insights into the design of cost-effective NO₃RR catalysts for water purification and environmental remediation.

Introduction

Anthropogenic activities such as fossil-fuel combustion, over-fertilization, and discharge of wastewater have caused an imbalance in the global nitrogen cycle, posing a major threat to the environment and public health.[1–3] Therefore, the World Health Organization (WHO) has stated that the nitrate concentration in public water systems should not exceed 10 mg L^{-1}.[4] Engineered reduction of excessive NO₃⁻ to benign dinitrogen (N₂) is becoming progressively essential. Among the current state-of-the-art denitrification methods, the electrocatalytic nitrate reduction reaction (NO₃RR) has been considered a promising way because of the high energy efficiency, moderate operating conditions, and no chemical input.[5–8]

Catalytic reduction capacity and selectivity for N₂ generation are vital factors for the NO₃RR. Many studies suggest that low-cost and nontoxic iron-based electrocatalysts exhibit high reduction ability in the conversion of NO₃⁻–N to NH₄⁺, which could be further converted to N₂ through the electrochlorination process around the anode.[9] A series of iron-based materials have been found to be active towards the NO₃RR, such as zero-valent iron, iron nitride, carbon-supported Fe–N$_x$/C compounds, iron-based bimetallic alloys, *etc.*[10–12] Recently, a new type of

[a] State Key Laboratory for Modification of Chemical Fibers and Polymer Materials, College of Materials Science and Engineering, Donghua University, Shanghai 201620, P. R. China. E-mail: jianpingyang@dhu.edu.cn

[b] Intelligent Polymer Research Institute, Australian Institute of Innovative Materials, Faculty of Engineering and Information Sciences, University of Wollongong, Wollongong, NSW 2522, Australia. E-mail: junc@uow.edu.au

[c] Department of Chemistry, City University of Hong Kong, Hong Kong SAR, China

† Electronic supplementary information (ESI) available. See DOI: https://doi.org/10.1039/d4ey00016a

iron-based catalyst Fe_3C, whose lattice contains carbon atoms located in trigonal prismatic interstices among close-packed iron atoms with space group $C(4c)$ (a = 5.032 Å, b = 6.708 Å, and c = 4.477 Å), has been reported as an ideal NO_3RR catalyst.[13,14] Such a crystalline structure leads to high activation of iron atoms on the carbide surface, making it an efficient catalyst toward accelerating the conversion of NO_3^-.[15] Furthermore, it has been confirmed that the metallic Fe_3C possesses small work functions, which are favorable for the charge transfer kinetics and beneficial for the NO_3RR performances.[16]

Nevertheless, phase-pure Fe_3C nanoparticles (NPs) inevitably undergo agglomeration and polydispersion during catalytic reactions, leading to the low catalytic capacity and durability. It has been confirmed that the NPs can be dispersed onto various solid substrates to enhance the accessibility of active sites. Numerous heterogeneous substrates, such as mesoporous carbon, graphene, carbon nanotubes, and carbon fibers, have been used to disperse NPs and regulate their particle size to create more active sites.[17,18] Compared with other carbon-based materials, N-doped carbon fibers are more attractive since the one-dimensional (1D) nanostructures could fully expose active-sites in the radial direction and promote charge transfer along the axial dimension in microns.[19,20] Furthermore, the uniform dissolution of the metal precursor in the electrospun solution enables good dispersion of metal species in the fiber matrix.[21] Previous studies have found that N-doping facilitates the adsorption of nitrate, and the continuous fibrous structure could enhance the stability of the catalyst and prevent the corrosion of the active sites.[22] However, the lack of interconnected pores leads to the poor exposure of NPs and thus results in lower catalytic activity. Therefore, constructing effective fiber-based electrocatalysts with tailored void space is considered vital for maximizing available active sites and facilitating mass transport.

Herein, we demonstrate the synthesis of uniformly dispersed Fe_3C NPs confined in multichannel nitrogen-doped carbon fibers ($Fe_3C/MNCFs$) via electrospinning and subsequent pyrolysis. The 1D hierarchical structure with highly parallel channels ensures good electrical contact between the catalyst and support, abundant active sites, and sufficient space for mass transfer. Moreover, the strong interaction between Fe_3C NPs and nitrogen-doped carbon fibers helps to stabilize Fe_3C NPs without aggregation or detachment. When used as the NO_3RR electrocatalyst, the $Fe_3C/MNCFs$ demonstrate ultrahigh nitrate conversion of 90.9% and nitrogen selectivity of 99.53%, and robust stability in neutral media. This strategy for the fabrication of a unique fibrous structure will open a new chapter in the development of highly efficient electrocatalysts for the NO_3RR.

Experimental

Preparation of electrospun nanofibers (PAN/PS/Fe(acac)$_3$)

In a typical synthesis, 600 mg PAN and 600 mg PS were added into 7 mL DMF with stirring overnight at room temperature to form a homogeneously dispersed solution. Then 200 mg of $Fe(acac)_3$ was added into the above solution with vigorous stirring for 6 h. Then, $PAN/PS/Fe(acac)_3$ nanofibers were electrospun on an Al foil collector from the precursor solution. The voltage, feeding rate, and the distance between the syringe and collector are fixed at 16 kV, 0.8 mL h^{-1}, 16 cm, respectively. The obtained electrospun nanofibers were dried at 60 °C overnight in a vacuum. Similarly, $Fe(acac)_3$ was also replaced with $Co(acac)_2$ and $Ni(acac)_2$ to synthesize a series of nanofibers, defined as $PAN/PS/Co(acac)_2$ and $PAN/PS/Ni(acac)_2$.

Synthesis of Fe$_3$C nanoparticle anchored multichannel carbon fibers (Fe$_3$C/MNCFs)

The as-obtained $PAN/PS/Fe(acac)_3$ nanofiber film was preoxidated in air at 200 °C for 4 h at a heating rate of 5 °C min^{-1}. After that, the $PAN/PS/Fe(acac)_3$ nanofiber film was annealed at 700, 800, 900 °C for 2 h under a H_2/Ar atmosphere with a ramp rate of 2 °C min^{-1} to form the $Fe_3C/MNCFs$.

Materials characterization

Scanning electron microscopy (SEM) images were taken using a TESCAN/MAIA3 (Czech Republic). Transmission electron microscopy (TEM) images and elemental mappings were obtained at 200 kV using a Talos F200S. X-ray diffraction (XRD) patterns were recorded using a Rigaku D/Max-2550 PC. Thermogravimetric analysis (TGA) was performed using NETZSCH STA449F5 apparatus under an air atmosphere. Raman spectra were recorded using a Dilor LabRam-1B Raman spectrometer with an excitation wavelength of 633 nm. X-ray photoelectron spectroscopy (XPS) was performed on an Escalab 250 Xi. The N_2 isothermal adsorption/desorption was recorded using a Quantachrome Autosorb-Iq. DMPO spin-trapping ESR spectra were obtained using a EMXnano (Germany). Thermogravimetric analysis (TGA) was performed using a NETZSCH STA449F5 system under an air atmosphere.

Electrocatalytic measurements

Electrochemical measurements were carried out by using a Bio-Logic VMP3 electrochemical analyzer system in a three-electrode cell. The platinum and saturated calomel electrodes were used as the counter and reference electrodes, respectively. To prepare the working electrode, 4 mg catalysts and 0.5 mg carbon black were dispersed in 50 μL, 10 wt% polyvinylidene fluoride, and sonicated for 10 min to form a homogenous ink. Then the ink was drop-cast on the nickel foam (1 × 1 cm) and dried at 70 °C under vacuum for 12 h.

Before the nitrate electroreduction test, linear sweep voltammetry (LSV) was performed until the polarization curves achieved a steady state at a rate of 10 mV s^{-1} from −0.5 to −2 V. Then, the potentiostatic test was carried out under different conditions, including applied potentials (−1.1, −1.2, −1.3, −1.4, and −1.5 V), electrolyte, and NO_3^-–N concentrations (25, 50, 100, 150, and 200 mg L^{-1}).

Determination of ion concentration

An ultraviolet-visible (UV-Vis) spectrophotometer was used to detect the ion concentration of pre- and post-test electrolytes after diluting to appropriate concentration to match the range of calibration curves. The specific detection methods from a previous work by our group are employed in this study.

Calculation of the nitrate conversion and N_2 selectivity

The nitrate conversion and N_2 selectivity were evaluated using the following equations:

$$\text{Conversion} = \frac{C(NO_3^- - N)_0 - C(NO_3^- - N)_t}{C(NO_3^- - N)_0} \times 100\%$$

$$\text{Selectivity} = \frac{\Delta C(NO_3^- - N)_0 - \Delta C(NO_2^- - N)_0 - \Delta C(NH_4^+ - N)_0}{\Delta C(NO_3^- - N)_0} \times 100\%$$

where $C(NO_3^- - N)_0$ is the initial concentration (mg L^{-1}) of $NO_3^- - N$, $C(NO_3^- - N)_t$ is the concentration (mg L^{-1}) of $NO_3^- - N$ at time t, and $\Delta C(NO_3^- - N)$, $\Delta C(NO_2^- - N)$, and $\Delta C(NH_4^+ - N)$ are the differences of $NO_3^- - N$, $NO_2^- - N$, and $NH_4^+ - N$ concentrations before and after the reaction, respectively. Nitrate removal capacities (Q) were calculated using the following equation: $Q = [C(NO_3^- - N)_0 - C(NO_3^- - N)_t]V/m_{Fe}$, where V (L) is the volume of nitrate solution and m_{Fe} (g) is the mass of iron in the composite coated on the nickel foam.

Computational methods

All the spin-polarized DFT calculations were performed with the Vienna ab initio simulation package (VASP) using the Perdew–Burke–Ernzerhof (PBE) functional within the generalized gradient approximation (GGA). The projected augmented wave (PAW) potentials were used to describe the ionic cores. A plane wave cut-off energy of 500 eV was applied for all the calculations. The criteria for force and electronic energy convergence are set to 0.01 eV Å^{-1} and 10^{-5} eV, respectively, during all the calculations. A Monkhorst–Pack mesh of $5 \times 4 \times 5$ was applied for structural relaxation of bulk Fe$_3$C. The Gaussian smearing with a smearing width was set as 0.10 eV.

The optimized lattice parameters of the bulk Fe$_3$C unit cell were a = 5.011 Å, b = 7.040 Å, and c = 4.672 Å, respectively. According to the high-resolution TEM image, the Fe$_3$C (210) surface was selected as the model, and a slab of five layers using a (1×3) supercell was cut from the bulk. The bottom two-layers were fixed for all calculations. A vacuum slab of 20 Å was built to avoid the interactions between periodic images. The dipole correction was adopted to remove the dipole interaction along the z direction. The DFT-D3 empirical correction method was used to describe van der Waals interactions. A Monkhorst–Pack mesh of $1 \times 1 \times 1$ was used for slab calculations. More computational details were followed from previous work.

Results and discussion

Synthesis and structural characterization of Fe$_3$C/MNCFs

The construction of Fe$_3$C/MNCFs was achieved by a facile electrospinning-calcination process, as shown in Fig. 1a. First, homogeneous solutions containing appropriate amounts of polyacrylonitrile (PAN), polystyrene (PS), and metal salts (Fe^{3+}, Co^{2+}, and Ni^{2+}) were used to synthesize the 1D fibrous structures through electrospinning. The PS could be stretched into nanoscaled wires in the PAN fibers during the electrospinning process, and then decomposed to generate nanochannels
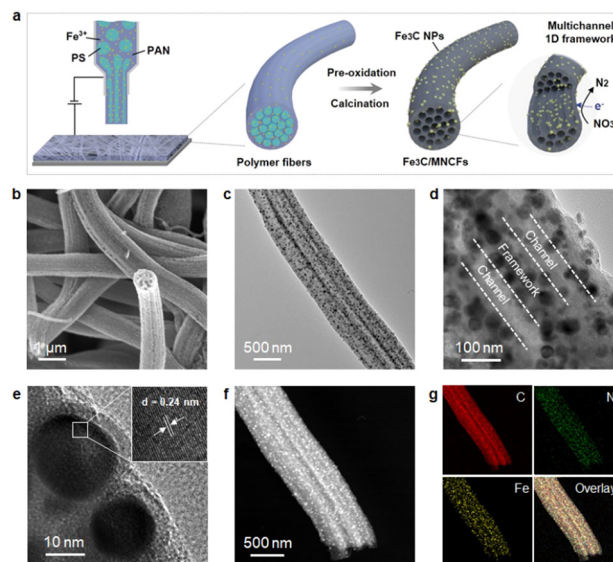

Fig. 1 (a) Illustration for the preparation of Fe$_3$C/MNCFs-800 via the electrospinning method and the subsequent pyrolysis. (b) SEM image of Fe$_3$C/MNCFs-800. (c) and (d) TEM images of Fe$_3$C/MNCFs-800. (e) HR-TEM image of Fe$_3$C/MNCFs-800. (f) HAADF-STEM image and (g) elemental mapping of Fe$_3$C/MNCFs-800.

during the pyrolysis process. Meanwhile, the metal precursors were reduced in situ to form nanoparticles embedded or anchored on the fiber skeleton. By adjusting the pyrolysis temperature from 700 to 900 °C, the 1D hierarchical structure with different skeleton structures and particle morphologies can be obtained.

The morphology and structure of Fe$_3$C/MNCFs were investigated by electron microscopy. The scanning electron microscopy (SEM) image showed that the obtained Fe$_3$C/MNCFs-800 maintained a continuous fibrous structure without obvious agglomeration or structural collapse (Fig. S1, ESI†). The cross-sectional SEM image demonstrates that Fe$_3$C NPs are homogenously anchored on the fiber skeleton with well-defined channels (Fig. 1b). The transmission electron microscopy (TEM) image further confirmed the 1D hierarchical structure of Fe$_3$C/MNCFs-800, consisting of plenty of well-dispersed Fe$_3$C NCs anchored on the hollow fiber inner wall and matrix (Fig. 1c and d). The HRTEM image in Fig. 1e demonstrated that the NPs were enclosed by carbon shells and the visible lattice fringe was 0.24 nm, corresponding to the (210) planes of the Fe$_3$C phase. The high-angle annular dark-field scanning transmission electron microscopy (HAADF-STEM) and elemental mapping images in Fig. 1f and g suggest that C, N and, Fe are evenly distributed within the entire Fe$_3$C/MNCFs-800. The energy-dispersive X-ray spectroscopy (EDS) line scans further verified that the Fe$_3$C NCs are distributed on the parallel channel walls and the fiber matrix (Fig. S2, ESI†).

Typical X-ray diffraction (XRD) patterns of the Fe$_3$C/MNCFs-x are shown in Fig. 2a. Apart from the broad diffraction hump at about 25° assigned to the (002) plane of graphitic carbon, the remaining sharp diffraction peaks can be indexed to metallic Fe$_3$C (JCPDS card no. 35-0772). Apparently, the intensity of Fe$_3$C peaks

increases with temperature, which can be attributed to the higher annealing temperature leading to the deeply reduced products with higher crystallinity. Raman analysis was carried out to determine the nature of the carbon fiber matrix (Fig. 2b). The two broad peaks of D and G bands at 1350 cm^{-1} and 1596 cm^{-1} correspond to the disordered defective carbon and the orderly graphitic carbon, respectively. The I_D/I_G ratio decreased with the increase of annealing temperature, indicating that high temperature can increase the degree of graphitization, which will contribute to better electronic conduction between the fiber skeleton and Fe$_3$C NPs.[23] N$_2$ adsorption–desorption analysis was performed to obtain the specific surface area and average pore size distribution of Fe$_3$C/MNCFs-x.[24] The specific surface area of Fe$_3$C/MNCFs-700, Fe$_3$C/MNCFs-800, and Fe$_3$C/MNCFs-900 is 37.5 m^2 g^{-1}, 138.8 m^2 g^{-1}, and 210.1 m^2 g^{-1}, respectively (Fig. 2c). This significant increment of the specific surface area is due to the increase of the nanopores. As shown in Fig. 2d, the average pore size of Fe$_3$C/MNCFs-800 is 4.84 nm, which is smaller than that of the Fe$_3$C/MNCFs-900 (6.40 nm). This indicated that high annealing temperature will accelerate the nucleation of Fe$_3$C NCs, thus leaving numerous nanopores in the fiber skeleton.

X-ray photoelectron spectroscopy (XPS) was used to elucidate the surface composition and binding structure of Fe$_3$C/MNCFs-800. The survey XPS spectra confirmed the co-existence of C, N, O, and Fe elements in Fe$_3$C/MNCFs-800 (Fig. S3a, ESI†). The high-resolution C 1s spectrum displays two deconvoluted

peaks at 286.2 and 284.8 eV, corresponding to the C–N/C–O and C=O species, respectively (Fig. S3b, ESI†).[25] The N 1s spectrum in Fig. 2e shows three peaks that are assigned to pyridinic-N (398.2 eV), pyrrolic-N (398.8 eV), and graphitic N (400.5 eV), confirming the successful doping of nitrogen into carbon fibers.[26] The high-resolution Fe 2p spectra show that all the iron can be attributed to Fe^{2+}/Fe^{3+} ionic species, confirming the existence of Fe$_3$C in the prepared Fe$_3$C/MNCFs-800 (Fig. 2f).[11]

The structures of Fe$_3$C/MNCFs-800 can be easily controlled by changing the applied voltage and weight ratio of PAN, PS, and Fe(acae)$_3$ (Fig. S4, ESI†). When the applied voltage increases, the Fe$_3$C/MNCFs exhibit a bead like structure (Fig. S4a and d, ESI†). As shown in Fig. S4b and e (ESI†), the uniformity of the fibrous structure deteriorates with the increase of Fe(acae)$_3$ content. An ideal support material should provide large internal space for high catalyst loading, so we attempted to change the weight ratio of PAN to PS to increase the number of inner channels. However, with the increase of the PS content, the decomposition of PS makes it impossible for PAN to form a continuous one-dimensional fiber skeleton (Fig. S4c and f, ESI†). Hence, all Fe$_3$C/MNCFs used in this work are fabricated according to the optimized PAN/PS/Fe(acae)$_3$ ratio of 3:3:1. Furthermore, the thermal carbonization temperature plays an important role in controlling the composition and morphology on the composite fibers. As the pyrolysis temperature increases from 700 to 900 °C, the particle size of Fe$_3$C increases gradually, leaving nanoholes in the fiber skeleton due to transformation of metal salts (Fig. S5, ESI†).

To demonstrate the adaptability of the approach, other metal salts (Co^{2+} and Ni^{2+}) were used to synthesize the 1D hierarchical structure. SEM and TEM images confirmed that the multichannel 1D structure we observed in Fe$_3$C/MNCFs could be well maintained when the Fe$_3$C was changed to Co (Fig. S6a and b, ESI†) and Ni (Fig. S6d and e, ESI†). Their XRD patterns clearly identify the consistent crystalline structure of Co/MNCFs-800 (JCPDS card no. 15-0806) and Ni/MNCFs-800 (JCPDS card no. 87-0712), as shown in Fig. S7 (ESI†). The uniform dispersion of different metals was further confirmed by STEM and elemental mapping images, suggesting the versatility of this method in synthesizing different metal-based channel-rich fibrous structures (Fig. S6c and f, ESI†).

Electrocatalytic performance toward the NO$_3$RR

The NO$_3$RR electrocatalytic activity of the Fe$_3$C/MNCFs was evaluated using a three-electrode system. The generated products were detected using ultraviolet-visible (UV/Vis) absorbance spectra (Fig. S8, ESI†). At −1.3 V, which was selected as the reaction potential, the Fe$_3$C/MNCFs-800 displayed superior NO$_3$RR performance (NO$_3^-$ conversion: 90.9% and N$_2$ selectivity: 99.53%) to Fe$_3$C/MNCFs-700 (NO$_3^-$ conversion: 46.3% and N$_2$ selectivity: 86.7%) and Fe$_3$C/MNCFs-900 (NO$_3^-$ conversion: 85.2% and N$_2$ selectivity: 97.77%) (Fig. 3a). Obviously, both the crystalline nature and well-defined multichannel fibrous structure synergistically promoted the catalytic performance of Fe$_3$C/MNCFs-800. Even though the Fe$_3$C/MNCFs-900 possess abundant nanopores for mass diffusion, the grain coarsening caused by high annealing

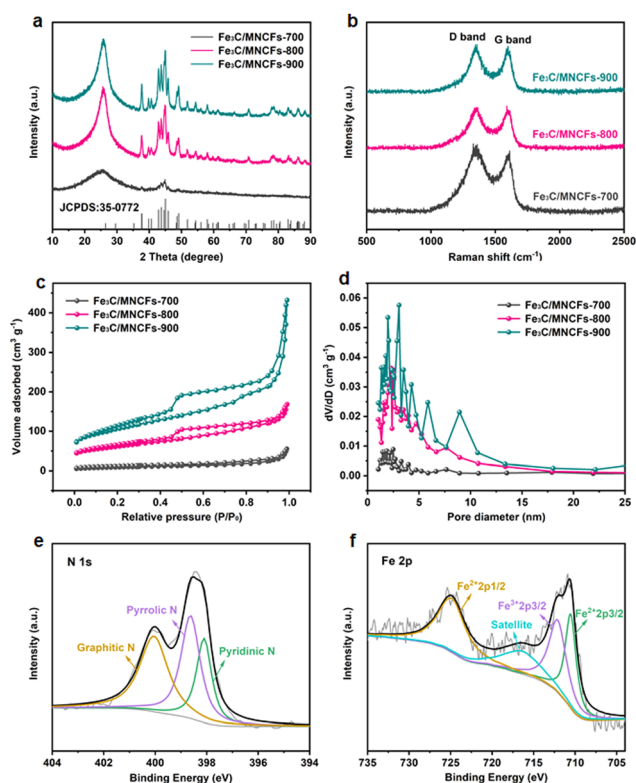Fig. 2 (a) XRD patterns, (b) Raman spectra, (c) nitrogen adsorption–desorption isotherms, and (d) pore diameter of Fe$_3$C/MNCFs with pyrolysis temperatures at 700 °C, 800 °C, and 900 °C. (e) N 1s and (f) Fe 2p spectra of Fe$_3$C/MNCFs-800.
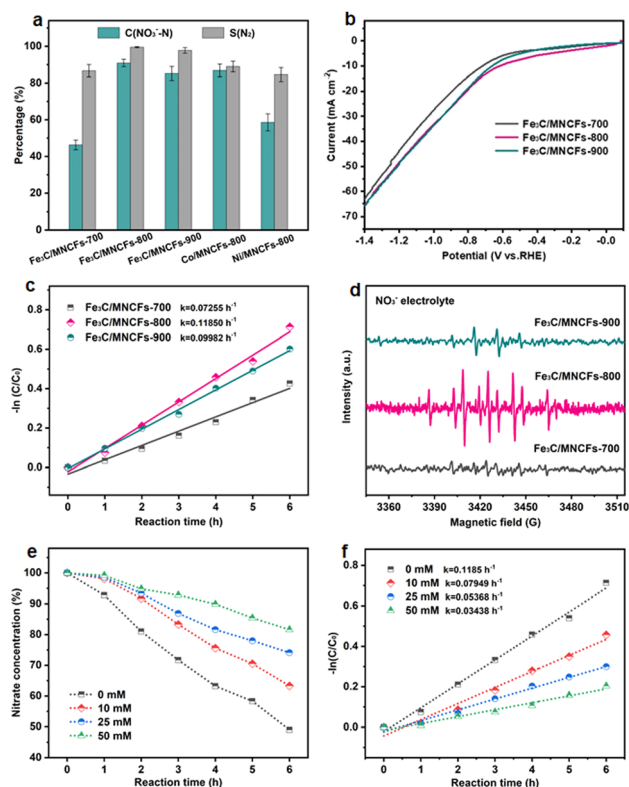
Fig. 3 (a) The comparison of the NO₃RR performance among different catalysts. (b) LSV curves of Fe₃C/MNCFs-*x* during nitrate electroreduction. (c) The linearized pseudo first-order kinetic profiles of Fe₃C/MNCFs-*x*. (d) DMPO spin-trapping ESR spectra of Fe₃C/MNCFs-*x*. (e) The change of nitrate concentration during the NO₃⁻RR process on Fe₃C/MNCFs-800 with different addition concentrations of TBA. (f) The linearized pseudo first-order kinetic profiles of Fe₃C/MNCFs-800 with different addition concentrations of TBA.

temperature inevitably leads to insufficient exposure of active sites. Moreover, the NO₃RR performance of Fe₃C/MNCFs-800 is significantly higher than that of Co/MNCFs-800 (NO₃⁻ conversion: 86.9% and N₂ selectivity: 88.98%) and Ni/MNCFs-800 (NO₃⁻ conversion: 58.6% and N₂ selectivity: 84.62%). Fig. 3b depicts the LSV linear sweep voltammetry (LSV) curves of different electrocatalysts. The Fe₃C/MNCFs-800 exhibited the strongest current density under reaction potential compared with Fe₃C/MNCFs-700 and Fe₃C/MNCFs-900, indicating obvious electroactivity of Fe₃C/MNCFs-800 for the NO₃RR.[27] The Fe₃C/MNCFs-800 displays significantly higher current density in 100 ppm of NO₃⁻ solution than in NO₃⁻ free solution, suggesting the occurrence of nitrate reduction rather than hydrogen evolution (Fig. S9, ESI†).[28] Chronoamperometry measurement testified that the Fe₃C/MNCFs-*x* can maintain a relatively stable current density at −1.3 V for 10 h. The Fe₃C/MNCFs-800 showed the highest current density at the same voltage, indicating the best electrocatalytic activity (Fig. S10, ESI†).

The kinetic analysis was further performed to reveal the catalytic process. According to the change of nitrate residues during the NO₃RR process, it can be seen that the reaction at Fe₃C/MNCFs-800 proceeded much faster than at other electrodes (Fig. S11, ESI†). The kinetics followed a pseudo first-order

rate law, and the apparent rate constants (k_{ap}) can be calculated through the slope of the linear fitting (Fig. 3c). For Fe₃C/MNCFs-800, the k_{ap} is higher than that of Fe₃C/MNCFs-700 and Fe₃C/MNCFs-900, indicating a faster reaction rate. Such a high reaction rate implies the existence of abundant available active sites, which make significant contributions to its optimized NO₃RR performance. To detect the presence of hydrogen radicals during the reaction process, the electron spin resonance (ESR) experiment was conducted using 5,5-dimethyl-1-pyrroline-*N*-oxide (DMPO) as a radical trapping reagent.[29] The ESR spectra exhibited nine characteristic peaks of DMPO-H with their intensity ratio close to $1:1:2:1:2:1:2:1:1$ (Fig. 3d). The strongest peak intensity of DMPO-H for Fe₃C/MNCFs-800 demonstrates the high active hydrogen adsorption capacity.[30]

Moreover, the *tert*-butyl alcohol (TBA), a specific quenching agent of hydrogen radicals, was used to identify the role of active hydrogen in the catalytic process.[31] As shown in Fig. 3e, the nitrate residue increases with the increase of TBA concentration. The k_{ap} of nitrate conversion decreased gradually when the TBA increased from 0 to 50 mM, indicating that the addition of TBA has a negative impact on nitrate reduction (Fig. 3f). The results showed that the active hydrogen plays a key role in catalytic reactions, and the high active hydrogen adsorption capacity of Fe₃C/MNCFs-800 is the main reason for its high activity.

The NO₃RR performance of Fe₃C/MNCFs-800 was evaluated under a variety of applied potential from −1.0 V to −1.5 V *vs.* SCE (Fig. 4a). The NO₃⁻ conversion rate increased with the increase of cathode potential, while the N₂ selectivity exhibited a volcanic trend. The increased NH₄⁺ selectivity was observed when the cathode potential exceeds −1.3 V, which is probably attributed to the Cl⁻ in the electrolyte not being sufficient to consume the excessive NH* generated around the electrode.

The effect of the evolution of NO₃⁻ and intermediate products (NO₂⁻, NH₄⁺, and N₂) on the performance of Fe₃C/MNCFs-800 was investigated to reveal the sequence of catalytic reactions over a reaction time of 24 h (Fig. 4b). The NO₃⁻ concentration decreased from the initial 100 ppm to the final 9.8 ppm, achieving a conversion efficiency of 90.2%. The NO₂⁻ was almost below the detection limit (0.001 ppm) during 24 h of the reaction, indicating that NO₂⁻ as an intermediate can be rapidly reduced to N₂ or NH₄⁺. The NH₄⁺ rapidly decreases within 4 to 6 h, and the residual amount is only 0.47% after 24 hours. The selectivity of N₂ was calculated to be 99.53% after 24 h on the basis of the N mass balance. The effect of the nitrate concentration on the catalytic performance was evaluated (Fig. 4c). The NO₃⁻ removal capacity was calculated based on the proportion of Fe₃C (14.55 wt%, according to the TGA result) (Fig. S12, ESI†). The NO₃⁻ removal capacity enhanced from 1064 to 7207 mg N g⁻¹ Fe₃C as the initial concentration of NO₃⁻–N increased from 25 to 200 ppm. The electrolyte showed significant influence on the conductivity and electrochemical reactions. To the best of our knowledge, the Na₂SO₄ can improve the NO₃⁻ conversion, while NaCl contributes to the selectivity of N₂. The iron-based electrocatalyst exhibited high reduction ability in the conversion of NO₃⁻–N to NH₄⁺, and the generated NH₄⁺–N can be converted into N₂ through the
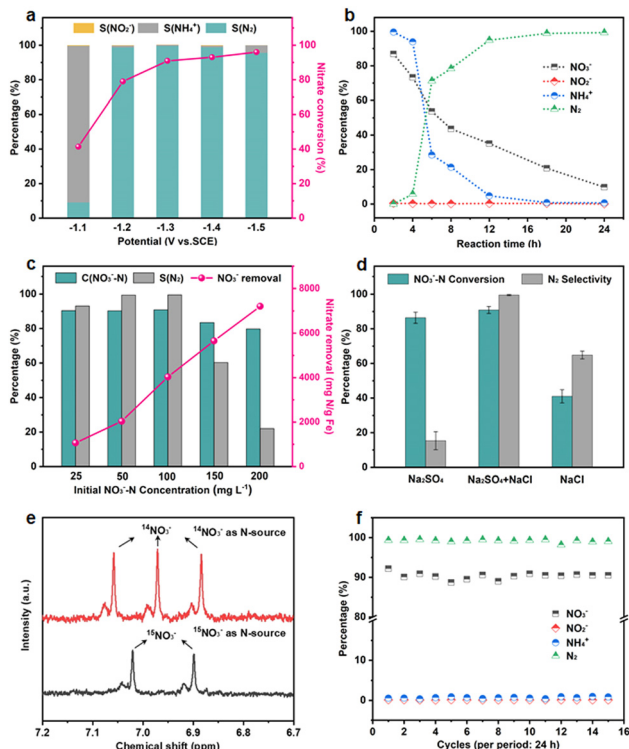
Fig. 4 (a) Nitrate conversion and product selectivity of Fe$_3$C/MNCFs-800 at different given potentials. (b) The evolution of NO$_3^-$, NO$_2^-$, NH$_4^+$, and N$_2$ of Fe$_3$C/MNCFs-800 for different reaction times. (c) Nitrate conversion, N$_2$ selectivity, and nitrate removal capacity of Fe$_3$C/MNCFs-800 at different initial NO$_3^-$−N concentrations. (d) Nitrate conversion and N$_2$ selectivity of Fe$_3$C/MNCFs-800 at different electrolytes. (e) ^{1}H NMR spectra of the electrolyte after the electrocatalytic NO$_3$RR using ^{14}NO$_3^-$ and ^{15}NO$_3^-$ as the nitrogen source. (f) Nitrate conversion and N$_2$ selectivity of Fe$_3$C/MNCFs-800 during 15 consecutive cycles. Reaction conditions: 0.1 M Na$_2$SO$_4$, 0.02 M NaCl, and −1.3 V, 24 h.

electrochlorination processes on the anode. In the Na$_2$SO$_4$ system, NO$_3^-$−N conversion reached 86.4% after 24 h of the reaction, while the N$_2$ selectivity was only 15.4% (Fig. 4d). In NaCl electrolyte, the N$_2$ selectivity (64.8%) is much higher than that in the Na$_2$SO$_4$ system, since NH$_4^+$ is oxidized to N$_2$ (2NH$_4^+$ + 3HClO → N$_2$ + 3H$_2$O + 3Cl$^-$ + 5H$^+$) by the generated HClO (Cl$_2$ + H$_2$O → HClO + Cl$^-$ + H$^+$).[32] In the mixed system, NO$_3^-$−N conversion is much higher than that of the single electrolyte, and the N$_2$ selectivity reaches almost 100%. These results indicated that the Na$_2$SO$_4$ accelerated NO$_3^-$ conversion while NaCl promoted the oxidation of NH$_4^+$ on the anode, leading to the simultaneously improved NO$_3^-$ removal efficiency and N$_2$ selectivity.[33] To verify the origin of ammonia and eliminate the possible interference from the external environment, a isotope-labeling test was conducted (Fig. 4e). It can be seen that the formation of ammonia originated from the electroreduction of nitrate.

The long-term stability was measured in the Na$_2$SO$_4$–NaCl system, and the NO$_3^-$−N conversion and N$_2$ selectivity almost remain unchanged during 15 test cycles, indicating the outstanding electrocatalytic stability of the Fe$_3$C/MNCFs-800
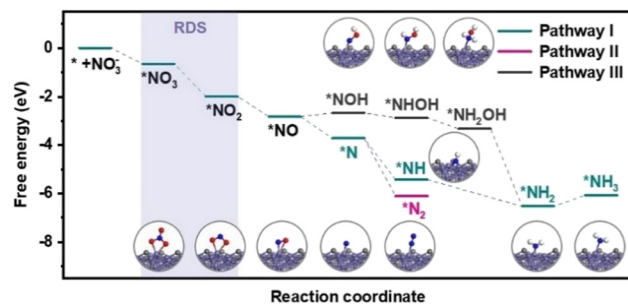

Fig. 5 Gibbs free energy diagrams for different NO$_3$RR pathways on Fe$_3$C/MNCFs.

(Fig. 4f). After consecutive electrocatalysis, the TEM images of the Fe$_3$C/MNCFs-800 exhibit the retained fibrous structure and well-dispersed nanoparticles (Fig. S13, ESI†). The strong anchoring effect enables the NPs stabilized on the fiber matrix without detachment and aggregation, while the thin carbon layer wrapped around Fe$_3$C NPs can prevent corrosion and leakage of active ingredients. The chemical states of Fe$_3$C/MNCFs-800 after the electrocatalytic nitrate reduction were identified by XPS. In Fig. S14 (ESI†), the Fe 2p spectrum shows that the new peak ascribed to Fe(0) appeared. The Fe(ɪ) in Fe$_3$C could be reduced to Fe(0) by the electrons and active hydrogen from the cathode, thus facilitating electron transfer and improving the reaction activity.

The reaction pathways of the NO$_3$RR and the free energy of each intermediate over Fe$_3$C/MNCFs were calculated using density functional theory (DFT) calculations (Fig. 5). Nitrate ions are first adsorbed on Fe$_3$C/MNCFs with a formation free energy change of −0.68 eV. After that, the N–O bond is continuously cleaved by proton-coupled electron transfer to form *NO$_2$ and *NO. Notably, the reduction of nitrate may occur in two cases after the production of *NO, that is, the *NOH pathway and *N pathway, respectively. From *NO to *NOH, the protonation of *NO → *NOH requires an energy uphill (ΔG = 0.16 eV). In contrast, the formation of *N species is more favourable with a free energy of −0.88 eV. Thus, pathway I and II are the favorable pathways for the nitrate reduction reaction. In pathway I, the *N undergoes a hydrogenation process to generate *NH$_3$, and the hypochlorite selectively oxidizes ammonia to N$_2$ through electrochlorination processes. Pathway II is more favorable in terms of the free energy change (ΔG = −2.40 eV) for N$_2$ production. This is highly consistent with the high selectivity of N$_2$ since the pathway II is thermodynamically barrierless compared with the other two paths.

Based on the electrochemical behavior analysis, the high catalytic performance of Fe$_3$C/MNCFs-800 can be attributed to not only the high activity of Fe$_3$C NPs but also the well-designed 1D architecture. The multi-channel 1D fiber support promotes the permeation of active species in the electrolyte as well as the mass diffusion, contributing to accelerating the reaction kinetics. Furthermore, the tight connection between the Fe$_3$C NPs and conductive MNCFs guarantees the structural stability and effective electronic pathways. Compared with the previous NO$_3$RR studies, Fe$_3$C/MNCFs-800 exhibits a high conversion efficiency

and N$_2$ selectivity that are superior or comparable to the performances of alloy or noble metal catalysts (Table S1, ESI†).[34–40]

Conclusions

In summary, multichannel nitrogen-doped carbon fiber confined Fe$_3$C NPs have been rationally designed and synthesized through a facile electrospinning method and a pyrolysis process. The hierarchical 1D architecture helps to maximize the utilization of effective active sites and to promote efficient electron transfer. Benefiting from the synergy between the multichannel fibrous structure and the strong interfacial interaction between the active species and supports, the obtained catalysts delivered a high nitrate conversion of 90.9% and nitrogen selectivity of 99.53%, as well as long-term stability. This work may provide new insights into the design of cost-effective NO$_3$RR catalysts for water purification and environmental remediation.

Author contributions

F.-Z. Z., and J.-P. Y. designed the studies. F.-Z. Z. synthesized the catalysts and performed the catalytic tests. Z.-S. S. performed the density functional theory calculations. F.-Z. Z., J.-L. C., and H.-X. L. conducted SEM, TEM, XRD, XPS, and TGA measurements. F.-Z. Z. wrote the paper with the help of J.-P. Y. and J. C. All authors discussed the results and commented on the manuscript.

Conflicts of interest

There are no conflicts to declare.

Acknowledgements

References

1 X. Zhang, B. B. Ward and D. M. Sigman, *Chem. Rev.*, 2020, **120**, 5308–5351.

2 Z. Chang, G. Meng, Y. Chen, C. Chen, S. Han, P. Wu, L. Zhu, H. Tian, F. Kong, M. Wang, X. Cui and J. Shi, *Adv. Mater.*, 2023, **35**, 2304508.

3 Y. Lv, S.-W. Ke, Y. Gu, B. Tian, L. Tang, P. Ran, Y. Zhao, J. Ma, J.-L. Zuo and M. Ding, *Angew. Chem., Int. Ed.*, 2023, **62**, e202305246.

4 A. S. Fajardo, P. Westerhoff, C. M. Sanchez-Sanchez and S. Garcia-Segura, *Appl. Catal., B*, 2021, **281**, 119465.

5 K. Chu, W. Zong, G. Xue, H. Guo, J. Qin, H. Zhu, N. Zhang, Z. Tian, H. Dong, Y.-E. Miao, M. B. J. Roeffaers, J. Hofkens, F. Lai and T. Liu, *J. Am. Chem. Soc.*, 2023, **145**, 21387–21396.

6 Y. Zhang, Y. Wang, L. Han, S. Wang, T. Cui, Y. Yan, M. Xu, H. Duan, Y. Kuang and X. Sun, *Angew. Chem., Int. Ed.*, 2023, **62**, e202213711.

7 H. Xu, Y. Ma, J. Chen, W.-X. Zhang and J. Yang, *Chem. Soc. Rev.*, 2022, **51**, 2710–2758.

8 X. Zhao, G. Hu, G.-F. Chen, H. Zhang, S. Zhang and H. Wang, *Adv. Mater.*, 2021, **33**, 2007650.

9 H. Yu, S. Qu, P.-R. Chen, K.-Q. Ou, J.-Y. Lin, Z.-H. Guo, L. Zheng, J.-K. Li, S. Huang, Y. Teng, L. Zou and J.-L. Song, *J. Hazard. Mater.*, 2022, **430**, 128351.

10 W. Teng, N. Bai, Y. Liu, Y. Liu, J. Fan and W.-X. Zhang, *Environ. Sci. Technol.*, 2018, **52**, 230–236.

11 W. Duan, G. Li, Z. Lei, T. Zhu, Y. Xue, C. Wei and C. Feng, *Water Res.*, 2019, **161**, 126–135.

12 Y. Liu and J. Wang, *Sci. Total Environ.*, 2019, **671**, 388–403.

13 M. Ma, S. You, W. Wang, G. Liu, D. Qi, X. Chen, J. Qu and N. Ren, *ACS Appl. Mater. Interfaces*, 2016, **8**, 32307–32316.

14 W. Zong, H. Gao, Y. Ouyang, K. Chu, H. Guo, L. Zhang, W. Zhang, R. Chen, Y. Dai, F. Guo, J. Zhu, Z. Zhang, C. Ye, Y.-E. Miao, J. Hofkens, F. Lai and T. Liu, *Angew. Chem., Int. Ed.*, 2023, **62**, e202218122.

15 X. Fan, Z. Peng, R. Ye, H. Zhou and X. Guo, *ACS Nano*, 2015, **9**, 7407–7418.

16 Y. Wang, L. Zhang, Y. Niu, D. Fang, J. Wang, Q. Su and C. Wang, *Green Chem.*, 2021, **23**, 7594–7608.

17 X. Ma, J. Zhong, W. Huang, R. Wang, S. Li, Z. Zhou and C. Li, *Chem. Eng. J.*, 2023, **474**, 145721.

18 J. Wang, W. Teng, L. Ling, J. Fan, W.-X. Zhang and Z. Deng, *Environ. Sci.: Nano*, 2020, **7**, 1496–1506.

19 F. Zhang, J. Luo, J. Chen, H. Luo, M. Jiang, C. Yang, H. Zhang, J. Chen, A. Dong and J. Yang, *Angew. Chem., Int. Ed.*, 2023, **62**, e202310383.

20 X. Cao, L. Zhao, B. Wulan, D. Tan, Q. Chen, J. Ma and J. Zhang, *Angew. Chem., Int. Ed.*, 2022, **61**, e202113918.

21 F. Zhang, J. Chen, G. G. Wallace and J. Yang, *Prog. Mater. Sci.*, 2023, **133**, 101069.

22 Y. Lan, H. Luo, Y. Ma, Y. Hua, T. Liao and J. Yang, *Nanoscale*, 2021, **13**, 10108–10115.

23 S.-H. Bae, J.-E. Kim, H. Randriamahazaka, S.-Y. Moon, J.-Y. Park and I.-K. Oh, *Adv. Energy Mater.*, 2017, **7**, 1601492.

24 J. Zheng, X. Chen, X. Zhong, S. Li, T. Liu, G. Zhuang, X. Li, S. Deng, D. Mei and J.-G. Wang, *Adv. Funct. Mater.*, 2017, **27**, 1704169.

25 H. Li, T. A. Ha, S. Jiang, C. Pozo-Gonzalo, X. Wang, J. Fang, P. C. Howlett and X. Wang, *Electrochim. Acta*, 2021, **377**, 138089.

26 J. Wang, Z. Deng, T. Feng, J. Fan and W.-X. Zhang, *Chem. Eng. J.*, 2021, **417**, 129160.

27 Z.-X. Ge, T.-J. Wang, Y. Ding, S.-B. Yin, F.-M. Li, P. Chen and Y. Chen, *Adv. Energy Mater.*, 2022, **12**, 2103916.

28 H. Liu, X. Lang, C. Zhu, J. Timoshenko, M. Rüscher, L. Bai, N. Guijarro, H. Yin, Y. Peng, J. Li, Z. Liu, W. Wang, B. R. Cuenya and J. Luo, *Angew. Chem., Int. Ed.*, 2022, **61**, e202202556.

29 J. Lu, X. Liu, H. Zhang, M. Fu, H. Zheng, Q. Chen and J. Zhou, *Chem. Eng. J.*, 2022, **433**, 134586.

30 C. Feng, W. Zhou, H. Wu, Q. Huo, J. Shao, X. Li, H. Yang, Q. Hu and C. He, *Appl. Catal., B*, 2024, **341**, 123280.

31 Y. Wang, H. Li, W. Zhou, X. Zhang, B. Zhang and Y. Yu, *Angew. Chem., Int. Ed.*, 2022, **61**, e202202604.

32 Y. Zhang, Y. Zhao, Z. Chen, L. Wang, P. Wu and F. Wang, *Electrochim. Acta*, 2018, **291**, 151–160.

33 J. Sun, W. Gao, H. Fei and G. Zhao, *Appl. Catal., B*, 2022, **301**, 120829.

34 H. Zhang, C. Wang, H. Luo, J. Chen, M. Kuang and J. Yang, *Angew. Chem., Int. Ed.*, 2023, **62**, e202217071.

35 X. Chen, T. Zhang, M. Kan, D. Song, J. Jia, Y. Zhao and X. Qian, *Environ. Sci. Technol.*, 2020, **54**, 13344–13353.

36 Y. Lan, J. Chen, H. Zhang, W.-X. Zhang and J. Yang, *J. Mater. Chem. A*, 2020, **8**, 15853–15863.

37 H. Luo, C. Wang, J. Wang, Y. Ma and J. Yang, *Inorg. Chem. Front.*, 2023, **10**, 4526–4533.

38 F. Ni, Y. Ma, J. Chen, W. Luo and J. Yang, *Chin. Chem. Lett.*, 2021, **32**, 2073–2078.

39 L. Su, D. Han, G. Zhu, H. Xu, W. Luo, L. Wang, W. Jiang, A. Dong and J. Yang, *Nano Lett.*, 2019, **19**, 5423–5430.

40 H. Luo, S. Li, Z. Wu, Y. Liu, W. Luo, W. Li, D. Zhang, J. Chen and J. Yang, *Adv. Mater.*, 2023, **35**, 2304695.